JGR Space Physics

RESEARCH ARTICLE
10.1029/2024JA033176

Impact of Interplanetary Shock on Thermospheric Cooling Emission: A Case Study

Tikemani Bag[1], **V. Sivakumar**[2,3], **and Y. Ogawa**[1]

[1]National Institute of Polar Research, Tokyo, Japan, [2]Discipline of Physics, University of KwaZulu-Natal, Durban, South Africa, [3]National Institute for Theoretical and Computational Sciences, University of KwaZulu-Natal, Durban, South Africa

Key Points:

- Response of thermospheric NO cooling emission to IP shock is studied during 26 January 2017
- The NO cooling emission shows a strong enhancement due to IP shock
- It can be attributed to the increase in low energy particle precipitation, NO density and thermospheric temperature

Correspondence to:

T. Bag,
tikemani.bag@nipr.ac.jp

Citation:

Bag, T., Sivakumar, V., & Ogawa, Y. (2024). Impact of interplanetary shock on thermospheric cooling emission: A case study. *Journal of Geophysical Research: Space Physics*, *129*, e2024JA033176. https://doi.org/10.1029/2024JA033176

Received 14 AUG 2024
Accepted 12 SEP 2024

Author Contributions:

Conceptualization: Tikemani Bag
Data curation: Tikemani Bag, Y. Ogawa
Formal analysis: Tikemani Bag
Investigation: Tikemani Bag
Methodology: Tikemani Bag
Software: Tikemani Bag
Supervision: V. Sivakumar, Y. Ogawa
Validation: Tikemani Bag
Visualization: Tikemani Bag, V. Sivakumar, Y. Ogawa
Writing – original draft: Tikemani Bag
Writing – review & editing: Tikemani Bag, V. Sivakumar, Y. Ogawa

Abstract Interplanetary (IP) shock is one of the most common phenomena that controls the shape and size of the magnetosphere. It affects the whole magnetosphere-ionosphere-thermosphere (MIT) system. We utilized the NO 5.3 μm radiative emission, as observed by SABER (Sounding of the Atmosphere using Broadband Emission Radiometry) onboard NASA's TIMED (Thermosphere Ionosphere Mesosphere Energetics Dynamics) satellite, to investigate its response to fast forward shock during 26 January 2017. The high latitude NO emission exhibits a strong enhancement (~three times with respect to pre-event value) during IP shock within 5 hr of onset. We analyzed both the energy dissipation sources and subsequent chemical mechanisms. The Field-Aligned-Current observations from Active Magnetosphere and Planetary Response Experiment (AMPERE), EISCAT measurements of Pederson conductivity and the defense Meteorological Satellite Program (DMSP F18) calculated hemispheric power demonstrate a strong intensification. The low energy particle precipitation from DMSP F18 spacecraft shows an early enhancement for energy less than 1 keV. The particle flux of higher energy responds later which remained elevated for longer duration. The thermospheric density and temperature also experience significant variation during IP shock. The NO molecule and temperature displayed an early enhancement. NO density increased by an order of magnitude with respect to the pre-event value. About 20% increase is noticed in the temperature variation. The atomic oxygen and atomic nitrogen illustrate an early depletion during IP event. The enhanced response of NO cooling to IP shock can be attributed to the combined effects of energy input and subsequent chemical mechanisms.

1. Introduction

Interplanetary (IP) shocks are rapid disturbances in the solar wind characterized by abrupt changes in its speed, density, and magnetic field orientation. The shocks are often created when a fast stream of solar wind overtakes a slower stream (Lui, 2011; Oliveira, 2017, 2023; Oliveira et al., 2024, and references therein). The abrupt change drives shock waves that propagate through the interplanetary medium. The IP shocks are classified into different categories depending on the relative speed of shock with respect to the ambient solar wind, and orientation of the interplanetary magnetic field (see, Oliveira, 2017). If the relative speed of the shock is greater (lower) than the ambient solar wind, the shock is known as fast (slow) shock. Similarly, the IP shock is called as fast forward shock (fast reverse shock) if the fast shock is moving away from (towards) the sun. The solar wind parameters such as plasma density, magnetic field, pressure and speed show enhancement during fast forward shocks (FFS). FFS are more frequent and are considered the most geoeffective. There occurs a decrease in solar wind dynamic pressure and density, increase in interplanetary magnetic field and solar wind speed during slow reverse shock. The slow reverse shocks (SRS) are rare and least geoeffective.

IP shock controls the shape, size and orientation of magnetosphere affecting whole magnetosphere-ionosphere-thermosphere (MIT) system. The compression of magnetosphere excites ultra-low frequency (ULF) waves, drives polar vortex and triggers the formation of auroral arc (Fujita, 2019; Fujita et al., 2004; Sato et al., 2001; Zhou et al., 2003). Oliveira et al. (2020) studied the impact of IP shocks on magnetospheric ULF wave activity. They revealed that the shock impact angle controls the amplitude, frequency, and power spectra of the ULF waves. Shocks with a more perpendicular impact angle excite stronger ULF waves with higher frequencies. The ULF waves interact with charged particles, accelerating them to high energies which penetrate into the upper atmosphere, causing increased ionization and heating leading to change in the electron density and conductivity of ionosphere affecting radio wave propagation and satellite communication (Oliveira, 2023; Oliveira et al., 2024, and references therein). The IP shock also results in the generation of ionospheric flow vortex and equatorial

expansion of auroral boundary due to the pitch angle diffusion of low energy particle precipitation and field aligned current. The flow vortex and auroral arc affect electron density and temperature variations (Cao et al., 2013; Fu et al., 2011; Liu et al., 2023; Shi et al., 2014; Yu et al., 2016; Zhou et al., 2003, and references therein).

The IP shock intensifies the field-aligned-current due to the expansion/compression of magnetosphere which strengthens the Joule heating rate and energetic particle precipitation (Bag & Ogawa., 2024a; Palmroth et al., 2004). By using ACE observations of solar wind data, AE index and GUMICS MHD simulation, Palmroth et al. (2004) reported an enhancement in Joule heating during positive pressure impulse event. Similarly, Bag and Ogawa. (2024a) studied the intensification of field-aligned-current and subsequent enhancements in the Joule heating rate and particle precipitation during a negative pressure impulse on 8 November 2010 by using numerical simulations and EISCAT measurements. Their study shows a delayed enhancement of NO emission to negative pressure impulse. It is well known that the Joule/Particle heating dictates the variation in neutral density, temperature and global circulation patterns. The radiative emission by Nitric Oxide (NO) 5.3 μm regulates the thermospheric temperature increase due to its radiative nature (Mlynczak et al., 2003). It is the dominating coolants in Earth's atmosphere above 100 km (Kockarts, 1980) and is closely related to the energy deposition during space weather events (Bag, 2018a, 2018b; Bag & Ogawa, 2024a, 2024b; Bag et al., 2014, 2020, 2023; Bharti et al., 2018; Knipp et al., 2013; Li et al., 2019; Mlynczak et al., 2003, 2024, and references therein).

The inelastic collision of NO with atomic oxygen density is the primary production source of NO emission. It excites NO density into higher vibrational levels. The low energy particle flux also plays important role in the formation of thermospheric NO density. The electron flux of energy 1–10 keV and ion flux of 10–20 keV dissociates N_2 into atomic nitrogen (N^4S, N^2D) which subsequently reacts with molecular oxygen to produce NO density (Barth, 2010; Barth et al., 2009; Richards., 2004). It is a significant source of NO density during space weather events. There are several studies of NO radiative emission during geomagnetic storm periods (Bag & Ogawa, 2024a; Knipp et al., 2013; Mlynczak et al., 2003, 2024, and references therein). However, there is little study on understanding the response of NO emission to IP shocks. For the first-time, we report the impacts of fast forward shock (FFS) on NO cooling emission during 26 January 2017 by using TIMED/SABER satellite observations. We divide this study into four sections. Section 2 describes the data acquisition and analysis methods. The response of NO emission to FFS IP is discussed in Section 3. Finally, we conclude the paper with summary in Section 4.

2. Data Analysis

SABER (Sounding of the Atmosphere using Broadband Emission Radiometry) is one of the four instruments onboard the TIMED (Thermosphere Ionosphere Mesosphere Energetics Dynamics) satellite. SABER is a limb sounder having 10 distinct spectral channels to measure radiance ($W.cm^{-2}.sr^{-1}$) from 1.27 μm to 16.9 μm emission. At any time it asymmetrically covers the hemisphere from 53° latitude in one hemisphere to 83° in another that changes in every 60–65 days (Mlynczak et al., 2003). During the present event, SABER was on north view mode and covered –53°S to 83°N latitude. The Nitric Oxide (NO) emission at 5.3 μm falls under the weak-line limit of radiative transfer. Consequently, an Abel inversion technique is applied to the limb radiance to calculate volume emission rate (VER). The vertical profile of NO VER, from 100 to 250 km, is integrated vertically to get radiative flux/cooling flux. The NO emission has uncertainty of about 15% (Mlynczak et al., 2010). In the present study we have used SABER version 2.0 data obtained via https://saber.gats-inc.com/data.php.

The Field-aligned-Current (FAC) is obtained from AMPERE (Active Magnetosphere and Planetary Electrodynamics Response Experiment). AMPERE uses the Iridium satellite constellations. It has the time resolution of 2 min with 10 min integration time (Anderson et al., 2000, 2014). The AMPERE/Iridium data are obtained via https://ampere.jhuapl.edu/.

The hemispheric power and low energy precipitating particle flux are obtained from the Defense Meteorological Satellite Program (DMSP) F18 satellite (Rich et al., 1985). DMSP is a polar satellite having an orbital period of about 100 min. It has a low particle sensor that measures auroral particle in 20 energy channels covering energy range of 30 eV to 30 keV. The electron and ion flux data are separated into three categories, less than 1 keV, 1–10 keV, and greater than 10 keV, in the present study. The particle flux deposited into northern and southern

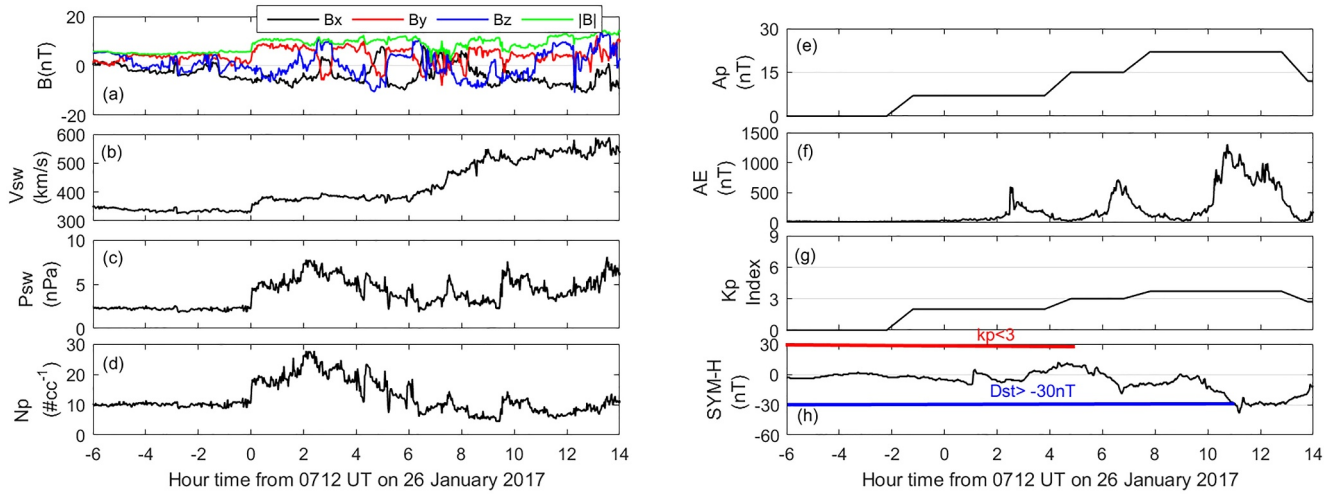

Figure 1. Time variation of (a) interplanetary magnetic field, (b) solar wind speed, (c) solar wind dynamic pressure, (d) solar wind density, (e) Ap index, (f) AE index, (g) Kp index and (h) SYM-H index during 26 January 2017. The solar and interplanetary data are obtained from WIND spacecraft. The Ap, AE, Kp, and SYM-H indices are from the OMNIWeb. Zero hour represents the onset time of IP shock. The horizontal red and blue lines, respectively, represent the time duration for Kp < 3 and SYM-H<| 30| nT, that is, period of geomagnetic quiet conditions.

hemispheres, above 45° magnetic latitude, provides the estimation of hemispheric power. The DMSP data are obtained via Madrigal database (http://millstonehill.haystack.mit.edu/).

The electron density, ion/electron temperature, ion velocity and the Pederson conductance are obtained from EISCAT UHF radar over Tromsø (geographic:69.59°N, 19.22°E; cgm:66.58°,102.94°), Norway, corresponding to common program mode (via https://eiscat.se/). The basic range and temporal resolution of measured ionospheric parameters above 70 km are determined by the selected pulse codes. The electric field is derived from tristatic measurements in the F-region, with the IGRF magnetic field model applied to the vertical drift. The electron density measurements along with altitudinal profiles of dominant (combined NO^+ and O_2^+, and O^+) ions are used to calculate Pederson conductivity in the altitude of 70–330 km with temporal resolution of 1-min and spatial resolution of 1 km (Brekke & Hall., 1988; Moen et al., 1990). The Pederson conductance, in northern hemisphere, is also calculated from DMSP spacecraft measurement following the formulation by Robinson et al. (1987) which is given as $\sigma_p = \frac{40\bar{E}}{16+\bar{E}^2}\Phi_E{}^{1/2}$, where $\bar{E}$ is the average energy in keV and Φ_E is the energy flux in ergs.cm^{-2}. s^{-1}.

The NO cooling emission depends on the NO density, thermospheric temperature and atomic oxygen density. In order to investigate the response to IP shock, the densities of NO, atomic oxygen, atomic nitrogen and thermospheric temperature are obtained from the NRLMSISE2.1 neutral atmosphere model (Emmert et al., 2022). The model data are sampled at the TIMED/SABER satellite measurement locations. They are, further, binned into 2 hr UT × 5° latitude grid to understand the temporal response across the latitude.

The interplanetary data along with the Akasofu parameter are obtained from the WIND spacecraft located at L1 Lagrangian point (via https://wind.nasa.gov/). Wind Magnetic Field Investigation (1 min) and Solar Wind Experiment (92 s) data are averaged to 92 s resolution in GSM coordinates. The Ap, Kp, AE, and SYM-H indices are from SPDF OMNIWeb database (via https://omniweb.gsfc.nasa.gov).

3. Results and Discussion

The solar and interplanetary magnetic field (IMF) along with SYM-H index data during 26 January 2017 are shown in Figure 1. The solar and IMF data are obtained from WIND spacecraft at L1 Lagrangian point. The Ap, Kp, AE and SYM-H indices are obtained from the OMNIWeb. The solar and interplanetary magnetic field data exhibit an abrupt change at 07:12 UT. This discontinuity in the solar wind parameters resulted-in the fluctuations in x, y, and z- components of IMF (Figure 1a). A strong elevation is observed in the solar wind parameters that remained elevated for longer duration. The solar wind speed increased significantly reaching the peak value of about 590 km/s, about 10–12 hr after the onset (Figure 1b). Similarly, the solar wind density and dynamic

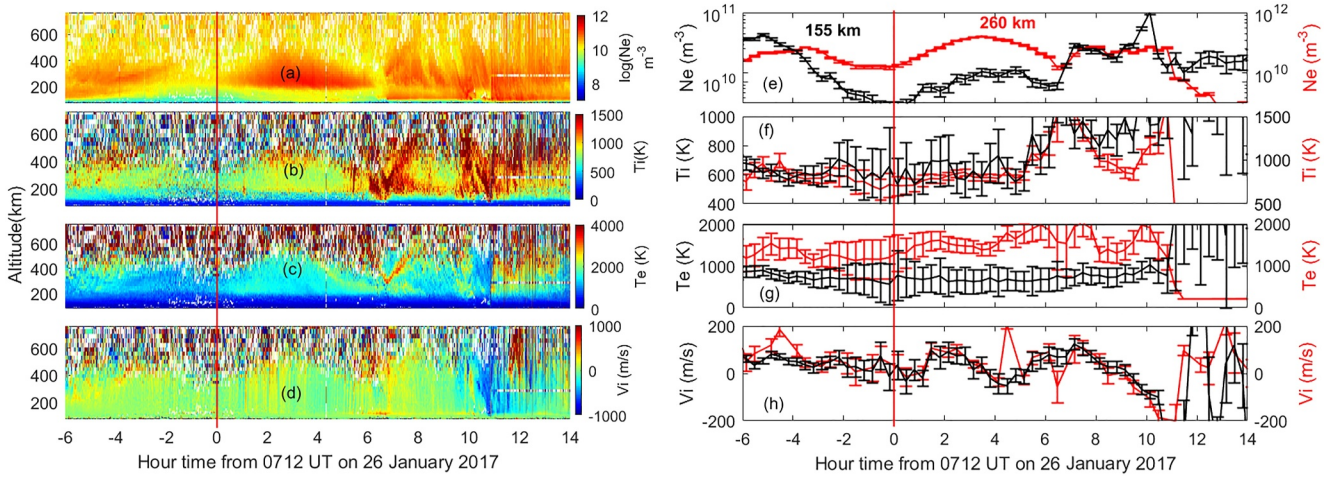

Figure 2. EISCAT measurements for the cross-sectional view of (a) electron density, (b) ion temperature, (c) electron temperature, (d) ion velocity, time variation of 20-min averaged (d) electron density, (e) electron temperature, (f) ion temperature and (h) ion velocity at 155 (black color) and 260 km (red color) during 26 January 2017 over Tromsø, Norway. The vertical red lines represent the onset of IP shock. Positive ion velocity (Vi) in (panel h) means away from EISCAT site.

pressure, respectively, reached the peak values of 28 cc^{-1} and 8 nPa within 2–3 hr (Figures 1c and 1d). The increase in all solar wind parameters (solar wind density, dynamic pressure, velocity and magnetic field) suggests the fast forward shock as the driver of this event. Surprisingly this event did not develop any significant geomagnetic storm on Earth till about +5 hr of IP shock (Figures 1e–1g). A minor storm (SYM-H < |40| nT) resulted after about 5 hr (see Ap, Kp, and SYM-H indices). The time duration for Kp index less than 3 and SYM-H index less than |30| nT are, respectively, shown by horizontal red and blue lines.

Figure 2 shows the EISCAT measurements of electron density, ion/electron temperature and ion velocity at Tromsø, Norway. The time-latitude cross-sectional views are shown in the left panels (Figures 2a–2d), whereas, their respective 20-min averaged variation at 155 km (black line) and 260 km (red line) are presented on right panels (Figures 2e–2h). The time variation of the electron density after the IP shock is due to the solar EUV illumination, so there is no clear change due to the IP shock. An increase in ion temperature (Ti) is observed intermittently after about 1 hr. An increase in electron temperature (Te) in the F region occurs continuously after about 4 hr of IP shock. The Te heating region extends from high latitude to low latitude. After 6 hr of IP shock there are significant changes in all parameters of temperature, velocity, density. This means that the ionospheric perturbation has spread to the surroundings of Tromsø. Please note that this EISCAT VHF radar was operated with low elevation north (elevation angle of 30°). A robust downward propagation of electron density is also observed all over the altitude region due to a minor storm superimposed over the preceding IP shock event. In response to the IP shock, changes in ion velocity due to electric field enhancement are observed continuously from about 1 hr. The IP shock induced electric field triggers in the enhanced velocity shear mapping into E region (Liu et al., 2023). The 20-min averaged electron/ion temperature and electron density undergo a significant enhancement due to IP shock (Figures 2e–2g). A slight delay with a strong directional change and intensification is observed in the ion velocity (Figure 3h). The increase in the ion velocity increases the Joule heating rate due to the square dependence on electric field.

The global response of NO emission to the fast forward shock is depicted in Figure 3. An increase in the NO volume emission rate along with peak altitude is observed due to IP shock (Figure 1a; see the circled area). The time-latitude cross-sectional view of NO cooling flux is shown in Figure 3b. The NO emission flux shows a smooth variation during pre-event period. It intensifies after the arrival of IP shock, particularly in high latitude region. The averaged pre-event NO flux is about 0.05 $mW.m^{-2}$. It increased by about three times reaching the value of 0.14 $mW.m^{-2}$ within 4–5 hr. However, maximum flux of about 0.3 $mW.m^{-2}$, in the high latitude region (~60–75°N), is observed after 10–12 hr of onset. It is about six times higher than the averaged pre-event value of 0.05 $mW.m^{-2}$. It is due to the combined effect of IP shock and a minor geomagnetic storm that resulted in subsequent time. A small increase also occurs in the southern hemisphere around the same time. It is due to the well-known traveling ionospheric disturbances that propagate equatorward as the time progresses. The temporal

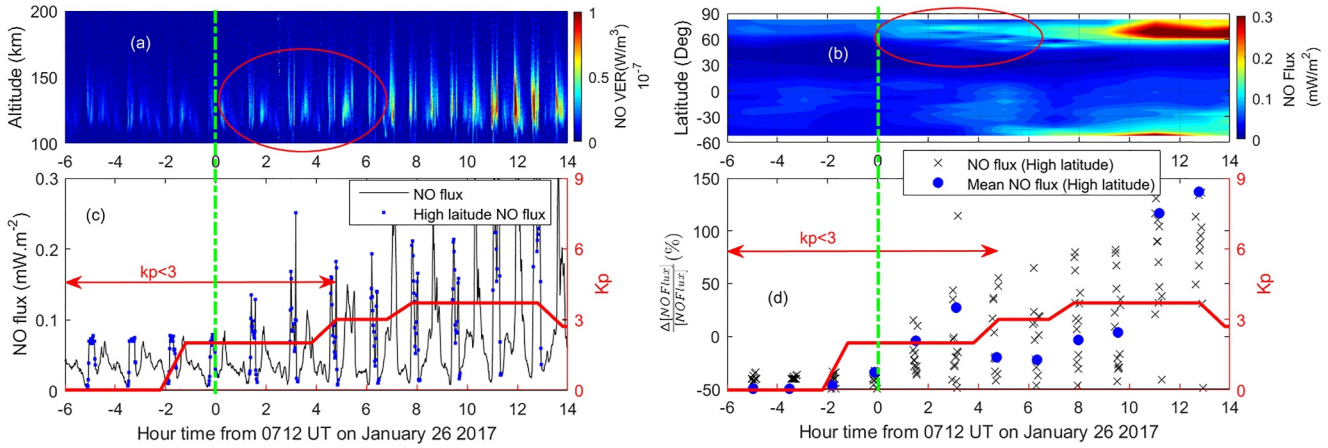

Figure 3. (a) Height-time variation of NO VER, (b) time-latitude cross-sectional view of NO cooling flux, (c) time variation of NO cooling flux and (d) relative change (%) in high latitude NO emission with respect to the mean value. The Kp index is overplotted. The vertical green lines represent the onset time of IP shock. The circled areas in panels (a) and (b) represent the area of increased emission. The blue dots (.) in panel (c) represent the high latitude NO flux. The circle in panel (d) represents the mean value. The horizontal red lines, in (panels c and d), represent the time of geomagnetic quiet period.

variation of NO flux along with the high latitude (latitude >60°N is considered as high latitude in the present study) variation is clearly noticeable in Figure 3c. The corresponding Kp index is shown to distinguish between geomagnetic quiet and active periods. The temporal variation illustrates a clear and distinct increment in NO flux during IP shock period. The average pre-event value is about 0.08 $mW.m^{-2}$. It increased to the average value of about 0.15 $mW.m^{-2}$ within 5 hr of IP shock. Figure 3d shows the relative change in high latitude NO cooling flux with respect to the mean value. The high latitude NO emission increases as shock progresses. It increases by about 50% the mean value within 5 hr of IP shock. It corresponds to the period of geomagnetic quiet condition suggesting the strong impact of fast forward IP shock. A maximum enhancement of more than 150% is observed with respect to the mean value due to the combined effect of IP shock and a minor geomagnetic storm.

The NO cooling emission has both direct and indirect sources. The abundances of NO, atomic oxygen and thermospheric temperature act as the direct sources. Whereas, the low energy particle precipitation and the Joule heating rate are the indirect sources. We explore both the sources to investigate the response of NO emission to IP shock.

Figure 4a shows the variation of Akasofu (ϵ) parameter obtained via https://wind.nasa.gov. It represents the solar wind energy deposition into Earth's magnetosphere (Akasofu., 1981; Koskinen & Tanskanen., 2002; Perreault & Akasofu, 1978). The Akasofu parameter increases significantly due to the IP shock suggesting huge amount of energy input into the Magnetosphere-Ionosphere-Thermosphere system. It shows a periodic energy deposition with peak within 10 hr of onset. The contraction of magnetosphere due to IP shock drives field-aligned-current, low energy particle precipitation by pitch angle diffusion, and generates flow vortex with equatorward expansion of auroral boundary (Jin et al., 2023; Zhou et al., 2003). The low energy particle precipitation creates Nitric Oxide via a series of chemical reaction mechanisms. The field-aligned-current affects the Joule heating rate. On the other hand, the flow vortex and auroral arc dictate the variation of electron density and electron/ion temperature (Jin et al., 2023; Lühr et al., 1996). Figure 3b shows the AMPERE/Iridium observations of field-aligned-current intensification in both hemispheres due to IP shock. However, it can be noticed that the field-aligned-currents (FACs) in northern hemisphere is higher than the southern hemispheric counterpart. Similar intensification of field-aligned-current due to IP shock-magnetosphere interaction has been reported earlier (Bag & Ogawa, 2024a; Belakhovsky & Vorobjev, 2016, and references therein). However, it can be noticed that FACs have strong phase difference with Akasofu parameter. It can be attributed to MLT dependence of FACs. Previous studies indicate that the response of the thermosphere-ionosphere system to interplanetary shocks (IPS) is highly dependent on local time and geographical location. For instance, Shi et al. (2017), using observations and OpenGGCM model simulations, reported that IPS leads to the formation and intensification of localized pairs of cusp field-aligned currents on the dayside due to reconnection following sudden magnetospheric compression. These FACs are initially localized in the prenoon and noon cusp areas, eventually extending azimuthally to merge with the

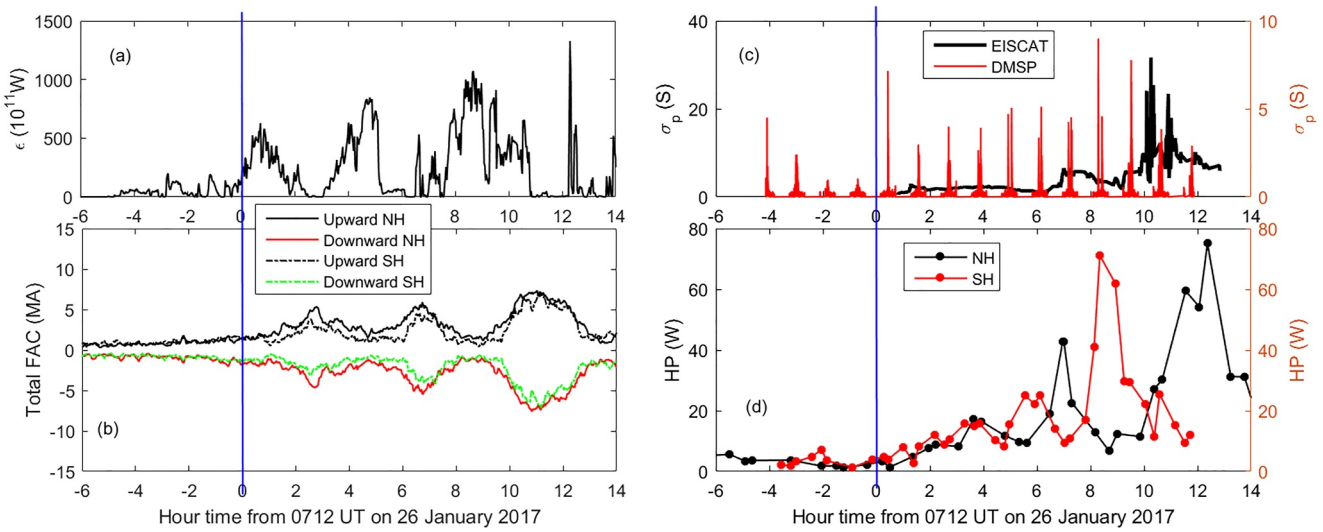

Figure 4. Temporal variation of (a) Akasofu parameter, (b) FACs, (c) Pederson conductance and (d) hemispheric power during 26 January 2017. Note the Pederson conductance from DMSP is only over the northern hemisphere.

enhanced Region 1 (R1) FAC system. Similarly, Bag and Ogawa. (2024a) demonstrated through AMPERE/Iridium observations a significant enhancement and equatorward propagation of prenoon and postnoon FACs during a slow reverse shock event on 8 November 2010. The field-aligned-current controls the Joule heating rate via Chapman-Ferraro current system and inner magnetospheric pressure (Palmroth et al., 2004) during positive pressure impulse when Z-component of IMF is southward. The Region 1 Field-Aligned Current (R1 FAC) regulates through the Chapman-Ferraro current system. Whereas, the Region 2 Field-Aligned Current (R2 FAC) affects via changes in inner magnetospheric pressure. This is due to the pressure balance between the lobe field and solar wind dynamic pressure, as well as between the lobe field and the plasma sheet. The increased dynamic pressure leads to a rise in inner magnetospheric pressure and a decrease in plasma sheet pressure (Palmroth et al., 2004). The enhancement in the Pederson conductance (as an indicator of Joule heating rate), obtained from EISCAT measurements and DMSP spacecraft, and hemispheric power can be seen from Figures 4c and 4d. The increase of ion velocity in Figures 2d and 2h suggests the intensification of east-west electric field. The DMSP derived Pederson conductance shows an early enhancement as compared to the EISCAT measurement. The hemispheric power shows a strong difference in response time; it is about 4–5 hr earlier in the southern hemisphere as compared to the northern hemispheric counterpart (Figure 4d). The difference in the behavior of Pederson conductance could be due to coverage of DMSP (F18 covers 08LT/20 LT) and localized EISCAT measurement. Earlier study by Shi et al. (2017) illustrated an intensification and azimuthal movement of Joule heating (JH) due to IPS, peaking near the noon region. Bag and Ogawa. (2024a) reported a strong increase in model simulation of Joule heating rate in the evening/morning sector that reached to about 60 magnetic latitude during a slow reverse shock event on 8 November 2010.

The low energy particles precipitating into Earth's atmosphere are shown in Figure 5. The particle flux is divided into three categories depending on the energy range; less than 1 keV, 1–10 keV and greater than 10 keV. The particle flux of all energy ranges undergoes strong increment. The electron and ion flux of energy of less than 1 keV undergo an early excessive enhancement during IP event. The particle flux of higher energy responds at later time. This time difference in the response of ion flux particularly of energy 1 keV remains poorly understood, necessitating further events to establish a comprehensive understanding. Zhou et al. (2003), by utilizing FAST and DMSP satellite observations, reported that electron energy precipitation increased significantly in the dawnside and duskside auroral ovals within approximately 10 min after a shock or pressure pulse. Further, they suggested that the structure of electron precipitation consisted of low-energy electrons (≤1 keV) at higher latitudes and high-energy electrons (1–10 keV) at lower latitudes, with a 1°–4° MLAT overlap along the boundary between Region 1 and 2 FACs. In addition, the precipitation of low-energy electrons has been reported to be associated with highly structured FACs, potentially generating electromagnetic broadband waves. Nonetheless, the electrons of energy less than 1 keV profoundly impacts NO cooling emission and immediately uplifts

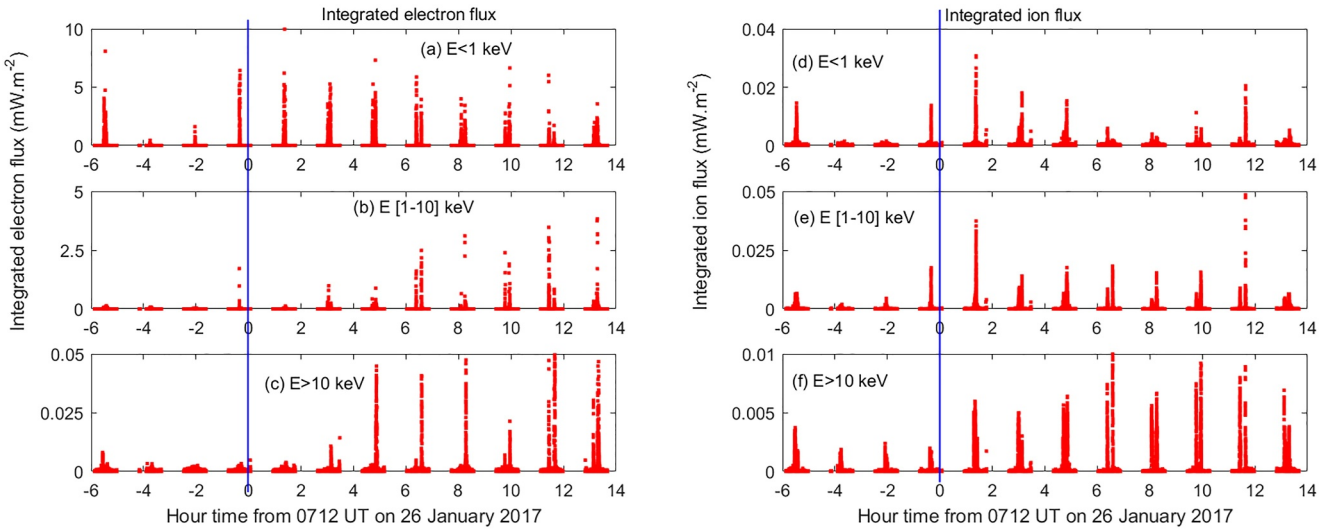

Figure 5. Time variation of integrated (a–c) electron flux and (d–f) ion flux during 26 January 2017 for different energy ranges.

thermospheric density (Knipp et al., 2013, 2017). The predominant source of thermospheric cooling emissions stems from electron energy flux within the 1.4–30 keV range, peaking notably between 1.4 and 3.1 keV. Electrons at 1 keV generate NO density above 120 km, while those within the 1.4–4.6 keV range deposit energy between 100 and 110 km. Ion contributions to NO density are also substantial. Galand et al. (1999) reported that ion energy flux ranging from 1 to 20 keV contributes over 50% of NO density in the nocturnal atmosphere. This process involves the dissociation of N_2 molecules into $N(^4S)$ and $N(^2D)$ by auroral electrons and ions, which subsequently react with molecular oxygen to form NO. A marked increase in particle flux would consequently lead to higher NO density production and NO cooling flux. An early and higher production of NO density during IP shock can be noticed from Figure 6a which depicts the time-latitude cross-section of NO density at 130 km. The densities of nitric oxide, atomic oxygen, atomic nitrogen and thermospheric temperature at different altitudes, obtained from NRLMSISE2.1 model sampled to the SABER location, are depicted in Figure 6. The uncertainties in NO, Atomic oxygen, atomic nitrogen and temperature are, respectively, about $\pm 30-50\%$, $\pm 20-30\%$, $\pm 30-50\%$, and $\pm 10-15$ K (Emmert et al., 2022). It is to be noted that the effectiveness of the AP index in capturing the impact of interplanetary shock events (using NRLMSISE) is not well established to the best of our knowledge. Figure 6a

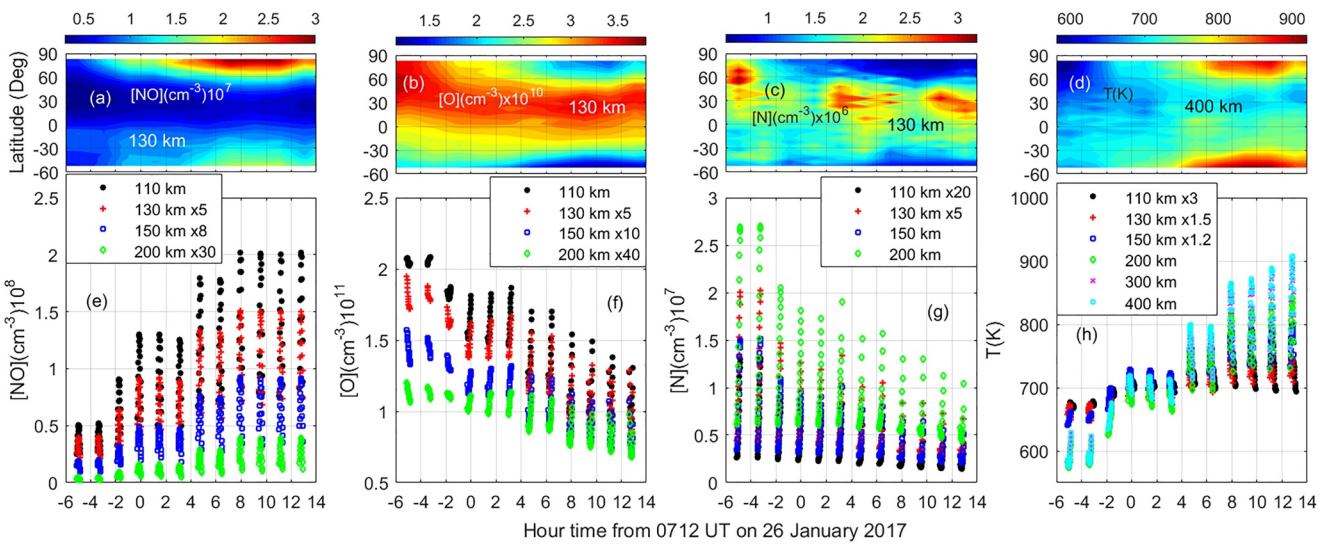

Figure 6. Time-latitude cross-section of (a) NO density, (b) atomic oxygen density, (c) atomic nitrogen density at 130 km and (d) temperature at 400 km. The temporal variation of high latitude (e) NO density, (f) atomic oxygen density, (g) atomic nitrogen density and (h) temperature at different altitudes.

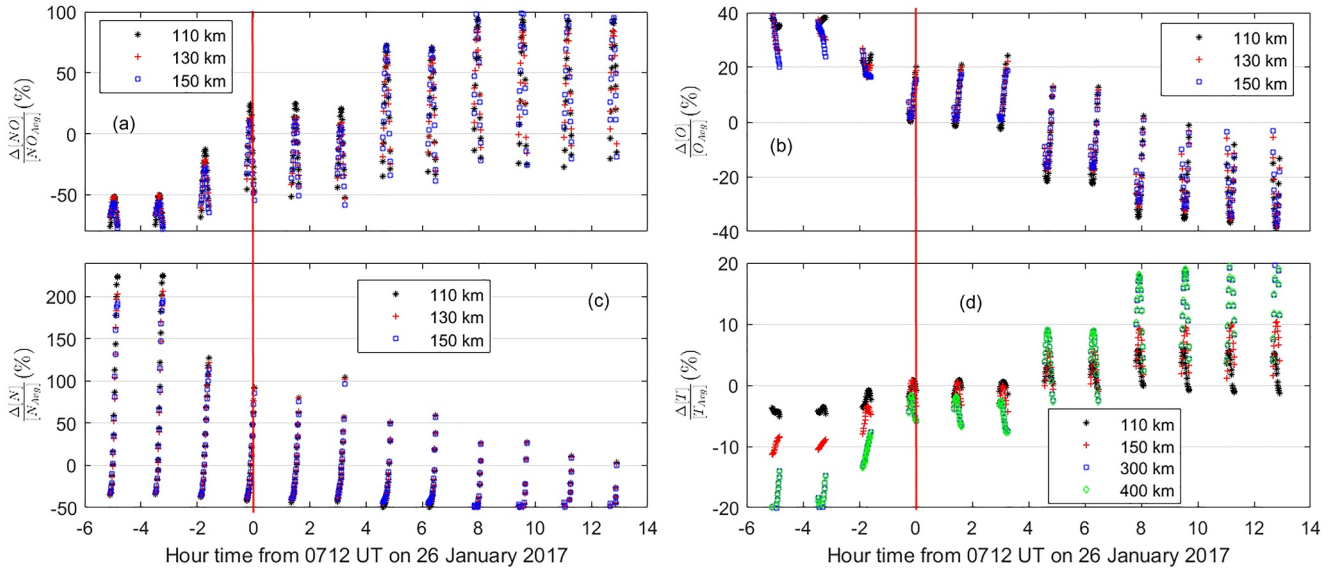

Figure 7. Relative change of high latitude (a) NO density, (b) atomic oxygen density, (c) atomic nitrogen density and (d) temperature with respect to averaged values at different altitude regions.

clearly shows a pre-event enhancement/higher production of NO density at northern high latitude that propagates toward the mid and low latitude regions. A small increase in NO density can also be noticed in southern hemisphere. Similar early depletion in atomic densities and a strong enhancement in thermospheric temperature can be noticed from Figures 6b–6d. Figures 6e–6h shows high latitude variation of densities and temperature at different altitude regions. The densities of NO, atomic oxygen and atomic nitrogen exhibit a stronger and early variation at lower altitude which decreases with increasing altitude. It is due to the decrease in the abundance of atmospheric density. On the other hand, higher altitude temperature exhibits an early and stronger enhancement as compared to the lower altitude.

Figure 7 shows the relative change of densities and temperature with respect to the respective averaged values at different altitude regions. NO density exhibits higher increase of about 100% with respect to the averaged value. It shows about 30% increase within 4 hr post-IP event period. Further, the enhancement is higher in the lower altitude region (Figure 7a). An opposite behavior is observed for atomic oxygen and atomic nitrogen densities (Figures 7b and 7c); atomic oxygen and nitrogen densities, respectively, deplete by about 40% and 50%. The temperature variation increases a maximum of 20% at 400 km. However, the atomic oxygen and atomic nitrogen increase, respectively, by about 20% and 50%, within 4 hr. Similar variation in densities and temperature has been reported by Bag and Ogawa. (2024c) using a superposed epoch study. No dramatic enhancement is noticed in thermospheric temperature within 4 hr although it tends to enhance afterward. The NO cooling emission linearly depends on the densities of NO and atomic oxygen, and non-linearly on thermospheric temperature (Mlynczak et al., 2003). The increase in the atomic oxygen density would result in the increase in NO emission. In addition, the increase in NO density and temperature would significantly increase NO cooling emission due to higher magnitudes which is clearly observed from Figure 3d. The EISCAT measurements also show a strong increase in ion/electron temperature due to IP shock (Figure 2). The strong increase in NO emission (three times within 4 hr of IP) with respect to the pre-event averaged value suggests a strong impact of IP shock on NO cooling emission.

4. Conclusions

Nitric Oxide emission at 5.3 μm wavelength is the dominant radiative coolant in the thermosphere above 100 km. We studied the impact of fast forward shock on NO emission during 26 January 2017 by utilized SABER measurements onboard the TIMED satellite. The salient features emerged from this investigation are as follows, (a) Low-energy particle precipitation exhibits an early and significant increase, (b) Particle flux at lower energies reacts more swiftly to interplanetary (IP) shocks as compared to higher energy flux, (c) There is a notable rise in nitric oxide (NO) density and thermospheric temperature along with a atomic oxygen density, (d) NO cooling

emission shows a pronounced response to IP shocks, increasing by about three times the pre-event average value, (e) The heightened NO emission response can be attributed to the combined effects of energy input and subsequent chemical processes.

Data Availability Statement

The authors thank TIMED/SABER science team for providing the data used in this study. The SABER data were downloaded from the SABER website via http://saber.gats-inc.com/data.php; then Access data >Browse data. The solar and IMF data are obtained from WIND spacecraft via https://wind.nasa.gov, then Plots and Data. The SYM-H index is from OMNIWeb (https://omniweb.gsfc.nasa.gov/, then High resolution OMNIWeb >Plots, listings, output files). The Field-Aligned-Current is obtained from AMPERE/Iridium satellite constellation via https://ampere.jhuapl.edu/, then Download. We thank the AMPERE team and the AMPERE Science Data Center for providing data products derived from the Iridium Communications constellation, enabled by support from the National Science Foundation. The low energy particle precipitation and hemispheric power are from DMSP F18 satellite via Madrigal database (http://millstonehill.haystack.mit.edu/, then Access Data> Single Experiment > Satellite Instruments > DMSP). The Pederson conductance is obtained from EISCAT measurement via https://portal.eiscat.se/schedule/.

Acknowledgments
The authors thank TIMED/SABER science team for providing the data used in this study. The SABER data were downloaded from the SABER website via http://saber.gats-inc.com/data.php. The solar and IMF data are obtained from WIND spacecraft via https://wind.nasa.gov. The SYM-H index is from OMNIWeb (https://omniweb.gsfc.nasa.gov/). The Field-Aligned-Current is obtained from AMPERE/Iridium satellite constellation (https://ampere.jhuapl.edu/). We thank the AMPERE team and the AMPERE Science Data Center for providing data products derived from the Iridium Communications constellation, enabled by support from the National Science Foundation. The low energy particle precipitation and hemispheric power are from DMSP F18 satellite via Madrigal database (http://millstonehill.haystack.mit.edu/). The Pederson conductance is obtained from EISCAT measurement via https://eiscat.se.

References

Akasofu, S.-I. (1981). Energy coupling between the solar wind and the magnetosphere. *Space Science Reviews*, *28*(2), 121. https://doi.org/10.1007/bf00218810

Anderson, B. J., Korth, H., Waters, C. L., Green, D. L., Merkin, V. G., Barnes, R. J., & Dyrud, L. P. (2014). Development of large-scale Birkeland currents determined from the active magnetosphere and planetary electrodynamics response experiment. *Geophysical Research Letters*, *41*(9), 3017–3025. https://doi.org/10.1002/2014GL059941

Anderson, B. J., Takahashi, K., & Toth, B. A. (2000). Sensing global Birkeland currents with iridium engineering magnetometer data. *Geophysical Research Letters*, *27*(24), 4045–4048. https://doi.org/10.1029/2000gl000094

Bag, T. (2018a). Diurnal variation of height distributed nitric oxide radiative emission during November 2004 super-storm. *Journal of Geophysical Research: Space Physics*, *123*(8), 6727–6736. https://doi.org/10.1029/2018ja025239

Bag, T. (2018b). Local-time hemispheric asymmetry in nitric oxide radiative emission during geomagnetic activity. *Journal of Geophysical Research: Space Physics*, *123*(11), 9669–9681. https://doi.org/10.1029/2018ja025731

Bag, T., Li, Z., & Rout, D. (2020). SABER observation of storm-time hemispheric asymmetry in nitric oxide radiative emission. *Journal of Geophysical Research: Space Physics*, *126*(4), e2020JA028849. https://doi.org/10.1029/2020ja028849

Bag, T., & Ogawa, Y. (2024a). Enhanced response of thermospheric cooling emission to negative pressure pulse. *Scientific Reports*, *14*(1), 9647. https://doi.org/10.1038/s41598-024-60471-2

Bag, T., & Ogawa, Y. (2024b). Response time of Joule heating rate and nitric oxide cooling emission during geomagnetic storms: Correlated ground-based and satellite observations. *Journal of Geophysical Research: Space Physics*, *129*(2), e2023JA032072. https://doi.org/10.1029/2023JA032072

Bag, T., & Ogawa, Y. (2024c). Impact of interplanetary shock on nitric oxide cooling emission: A superposed epoch study. *Advances in Space Research*. https://doi.org/10.1016/j.asr.2024.08.005

Bag, T., Rout, D., Ogawa, Y., & Singh, V. (2023). Distinctive response of thermospheric cooling to ICME and CIR-driven geomagnetic storms. *Frontiers in Astronomy and Space Sciences*, *10*. https://doi.org/10.3389/fspas.2023.1107605

Bag, T., Sunil Krishna, M. V., Gahlot, S., & Singh, V. (2014). Effect of severe geomagnetic storm conditions on atomic oxygen greenline dayglow emission in mesosphere. *Advances in Space Research*, *53*(8), 1255–1264. https://doi.org/10.1016/j.asr.2014.01.031

Barth, C. A. (2010). Joule heating and nitric oxide in the thermosphere. *Journal of Geophysical Research*, *115*(A10), A10305. https://doi.org/10.1029/2010JA015565

Barth, C. A., Lu, G., & Roble, R. G. (2009). Joule heating and nitric oxide in the thermosphere. *Journal of Geophysical Research*, *114*(A5), A05301. https://doi.org/10.1029/2008JA013765

Belakhovsky, V. B., & Vorobjev, V. G. (2016). Response of the night aurora to a negative sudden impulse. *Geomagnetism and Aeronomy*, *56*(6), 694–705. https://doi.org/10.1134/s0016793216060037

Bharti, G., Sunil Krishna, M. V., Bag, T., & Jain, P. (2018). Storm-time variation of radiative cooling by nitric oxide as observed by TIMED-SABER and GUVI. *Journal of Geophysical Research: Space Physics*, *123*, 1500–1514. https://doi.org/10.1002/2017JA024576

Brekke, A., & Hall, C. (1988). Auroral ionospheric quiet summer time conductance. *Annales de Geophysique*, *6*, 361–375.

Cao, J. B., Duan, A., Reme, H., & Dandouras, I. (2013). Relations of the energetic proton fluxes in the central plasma sheet with solar wind and geomagnetic activities. *Journal of Geophysical Research: Space Physics*, *118*(11), 7226–7236. https://doi.org/10.1002/2013JA019289

Emmert, J. T., Jones, M., Jr., Siskind, D. E., Drob, D. P., Picone, J. M., Stevens, M. H., et al. (2022). NRLMSIS 2.1: An empirical model of nitric oxide incorporated into MSIS. *Journal of Geophysical Research: Space Physics*, *127*(10), e2022JA030896. https://doi.org/10.1029/2022JA030896

Fu, H. S., Cao, J. B., Yang, B., & Lu, H. Y. (2011). Electron loss and acceleration during storm time: The contribution of wave-particle interaction, radial diffusion, and transport processes. *Journal of Geophysical Research*, *116*(A10), A10210. https://doi.org/10.1029/2011JA016672

Fujita, S. (2019). Response of the magnetosphere-ionosphere system to sudden changes in solar wind dynamic pressure. *Reviews of Modern Plasma Physics*, *3*(2), 2. https://doi.org/10.1007/s41614-019-0025-1

Fujita, S., Tanaka, T., Kikuchi, T., & Tsunomura, S. (2004). A numerical simulation of a negative sudden impulse. *Earth Planets and Space*, *56*(4), 463–472. https://doi.org/10.1186/bf03352499

Galand, M., Roble, R. G., & Lummerzheim, D. (1999). Ionization by energetic protons in thermosphere–ionosphere electrodynamics general circulation model. *Journal of Geophysical Research*, *104*(A12), 27973–27989. https://doi.org/10.1029/1999JA900374

Jin, Y., Moen, J. I., Spicher, A., Liu, J., Clausen, L. B. N., & Miloch, W. J. (2023). Ionospheric flow vortex induced by the sudden decrease in the solar wind dynamic pressure. *Journal of Geophysical Research: Space Physics*, *128*(11), e2023JA031690. https://doi.org/10.1029/2023JA031690

Knipp, D. J., Kilcommons, L., Hunt, L., Mlynczak, M., Pilipenko, V., Bowman, B., et al. (2013). Thermospheric damping response to sheath-enhanced geospace storms. *Geophysical Research Letters*, *40*(7), 1263–1267. https://doi.org/10.1002/grl.50197

Knipp, D. J., Pette, D. V., Kilcommons, L. M., Isaacs, T. L., Cruz, A. A., Mlynczak, M. G., et al. (2017). Thermospheric nitric oxide response to shock-led storms. *Space Weather*, *15*(2), 325–342. https://doi.org/10.1002/2016sw001567

Kockarts, G. (1980). Nitric oxide cooling in the terrestrial thermosphere. *Geophysical Research Letters*, *7*(2), 137–140. https://doi.org/10.1029/gl007i002p00137

Koskinen, H. E. J., & Tanskanen, E. (2002). Magnetospheric energy budget and the epsilon parameter. *Journal of Geophysical Research*, *107*(A11), 1415. https://doi.org/10.1029/2002JA009283

Li, Z., Knipp, D., & Wang, W. (2019). Understanding the behaviors of thermospheric nitric oxide cooling during the 15 May 2005 geomagnetic storm. *Journal of Geophysical Research: Space Physics*, *124*(3), 2113–2126. https://doi.org/10.1029/2018ja026247

Liu, J., Chakraborty, S., Chen, X., Wang, Z., He, F., Hu, Z., et al. (2023). Transient response of polar-cusp ionosphere to an interplanetary shock. *Journal of Geophysical Research: Space Physics*, *128*(3), e2022JA030565. https://doi.org/10.1029/2022JA030565

Lühr, H., Lockwood, M., Sandholt, P. E., Hansen, T. L., & Moretto, T. (1996). Multi-instrument ground-based observations of a travelling convection vortices event. *Annales de Geophysique*, *14*(2), 162–181. https://doi.org/10.1007/s00585-996-0162-z

Lui, A. T. Y. (2011). *Interplanetary shocks: Observations, mechanisms, and consequences*. Springer Science and Business Media.

Mlynczak, M. G., Hunt, L., Nowak, N., Marshall, B. T., & Mertens, C. J. (2024). Infrared radiation in the thermosphere from 2002 to 2023. *Geophysical Research Letters*, *51*(14), e2024GL109470. https://doi.org/10.1029/2024GL109470

Mlynczak, M. G., Hunt, L. A., Thomas Marshall, B., Martin-Torres, F. J., Mertens, C. J., Russell, J. M., III., et al. (2010). Observations of infrared radiative cooling in the thermosphere on daily to multiyear timescales from the TIMED/SABER instrument. *Journal of Geophysical Research*, *115*(A3), A03309. https://doi.org/10.1029/2009JA014713

Mlynczak, M. G., Martin-Torres, F. J., Russell, J., Beaumont, K., Jacobson, S., Kozyra, J., et al. (2003). The natural thermostat of nitric oxide emission at 5.3 μm in the thermosphere observed during the solar storms of April 2002. *Geophysical Research Letters*, *30*(21), 2100. https://doi.org/10.1029/2003GL017693

Moen, J., Brekke, A., & Hall, C. (1990). An attempt to derive electron energy spectra for auroral daytime precipitation events. *Journal of Atmospheric and Terrestrial Physics*, *52*(6), 459–471. https://doi.org/10.1016/0021-9169(90)90045-o

Oliveira, D. M. (2017). Magnetohydrodynamic shocks in the interplanetary space: A theoretical review. *Brazilian Journal of Physics*, *47*(1), 81–95. https://doi.org/10.1007/s13538-016-0472-x

Oliveira, D. M. (2023). Geoeffectiveness of interplanetary shocks controlled by impact angles: Past research, recent advancements, and future work. *Frontiers in Astronomy and Space Sciences*, *10*. https://doi.org/10.3389/fspas.2023.1179279

Oliveira, D. M., Hartinger, M. D., Xu, Z., Zesta, E., Pilipenko, V. A., Giles, B. L., & Silveira, M. V. D. (2020). Interplanetary shock impact angles control magnetospheric ULF wave activity: Wave amplitude, frequency, and power spectra. *Geophysical Research Letters*, *47*(24), e2020GL090857. https://doi.org/10.1029/2020gl090857

Oliveira, D. M., Zesta, E., & Vidal-Luengo, S. (2024). First direct observations of interplanetary shock impact angle effects on actual geomagnetically induced currents: The case of the Finnish natural gas pipeline system. *Frontiers in Astronomy and Space Sciences*, *11*, 2024. https://doi.org/10.3389/fspas.2024.1392697

Palmroth, M., Pulkkinen, T. I., Janhunen, P., McComas, D. J., Smith, C. W., & Koskinen, H. E. J. (2004). Role of solar wind dynamic pressure in driving ionospheric Joule heating. *Journal of Geophysical Research*, *109*(A11), A11302. https://doi.org/10.1029/2004JA010529

Perreault, P., & Akasofu, S. I. (1978). A study of geomagnetic storms. *Geophysical Journal International*, *54*(3), 547–573. https://doi.org/10.1111/j.1365-246x.1978.tb05494.x

Rich, F. J., Hardy, D. D., & Gussenhoven, M. S. (1985). Enhanced ionosphere–magnetosphere data from the DMSP satellites. *Eos, Transactions American Geophysical Union*, *66*(26), 513–514. https://doi.org/10.1029/eo066i026p00513

Richards, P. G. (2004). On the increases in nitric oxide density at midlatitudes during ionospheric storms. *Journal of Geophysical Research*, *109*(A6), A06304. https://doi.org/10.1029/2003JA010110

Robinson, R. M., Vondrak, R. R., Miller, K., Dabbs, T., & Hardy, D. (1987). On calculating ionospheric conductance from the flux and energy of precipitating electrons. *Journal of Geophysical Research*, *92*(A3), 2565–2569. https://doi.org/10.1029/ja092ia03p02565

Sato, N., Murata, Y., Yamagishi, H., Yukimatu, A. S., Kikuchi, M., Watanabe, M., et al. (2001). Enhancement of optical aurora triggered by the solar wind negative impulse (SI-). *Geophysical Research Letters*, *28*(1), 127–130. https://doi.org/10.1029/2000gl003742

Shi, Q. Q., Hartinger, M., Angelopoulos, V., Tian, A., Fu, S., Zong, Q., et al. (2014). Solar wind pressure pulse-driven magnetospheric vortices and their global consequences. *Journal of Geophysical Research: Space Physics*, *119*(6), 4274–4280. https://doi.org/10.1002/2013ja019551

Shi, Y., Zesta, E., Connor, H. K., Su, Y., Sutton, E. K., Huang, C. Y., et al. (2017). High-latitude thermosphere neutral density response to solar wind dynamic pressure enhancement. *Journal of Geophysical Research: Space Physics*, *122*(11), 11559–11578. https://doi.org/10.1002/2017JA023889

Yu, J., Li, L., Cao, J. B., Reeves, G. D., Baker, D. N., & Spence, H. (2016). The influences of solar wind pressure and interplanetary magnetic field on global magnetic field and outer radiation belt electrons. *Geophysical Research Letters*, *43*(14), 7319–7327. https://doi.org/10.1002/2016gl069029

Zhou, X. Y., Strangeway, R. J., Anderson, P. C., Sibeck, D. G., Tsurutani, B. T., Haerendel, G., et al. (2003). Shock aurora: FAST and DMSP observations. *Journal of Geophysical Research*, *108*(A4), 8019. https://doi.org/10.1029/2002ja009701